Supplementary Information for

Ferroelastic-switching-driven large shear strain and piezoelectricity in a hybrid ferroelectric

Yuzhong Hu[1,2,†], Lu You[3,†], Bin Xu[3,†], Tao Li[2], Samuel Alexander Morris[5], Yongxin Li[6], Yehui Zhang[3], Xin Wang[3], Pooi See Lee[2], Hong Jin Fan[1,*] and Junling Wang[2,4,*]

[1]School of Physical and Mathematical Sciences, Nanyang Technological University, Singapore 637371

[2]School of Materials Science and Engineering, Nanyang Technological University, Singapore 639798

[3]Jiangsu Key Laboratory of Thin Films, School of Physical Science and Technology, Soochow University, 1 Shizi Street, Suzhou 215006, China

[4]Department of Physics, Southern University of Science and Technology, Shenzhen 518055, China

[5]Facility for Analysis, Characterisation, Testing and Simulation (FACTS), Nanyang Technological University, Singapore, 639798

[6]Division of Chemistry and Biological Chemistry, School of Physical and Mathematical Sciences, Nanyang Technological University, Singapore 637371

†These authors contributed equally to this work.

*Corresponding author. Email: jwang@sustech.edu.cn (J.W.); fanhj@ntu.edu.sg (H.J.F.)

This PDF file includes:

Table of Contents

Supplementary Text

Supplementary Text 1 | Phase transition, crystallographic analysis and ferroelectric characterizations

Phase transition and crystallographic analysis

TGA was carried out on single crystals to investigate the decomposition temperatures of the (PTMA)$CdBr_{3x}Cl_{3(1-x)}$ solid solution (**Supplementary Fig. S2a**). The data indicate that they are thermally stable up to ~180 °C. DSC was then performed to study the phase transitions of the crystals during heating and cooling cycles (**Supplementary Fig. S2b** and **c**). With increasing Br amount, the transition temperature of the crystal decreases from above decomposition temperature (180 °C) to 19 °C (**Supplementary Fig. S2d**). In addition, thermal hysteresis becomes larger with higher Br amount, which rises from ~ 7 °C to ~ 30 °C for Br amount increasing from 63 % to 100 %.

Crystal structures of pure (**Supplementary Fig. S3**) and 76 % Br (**Supplementary Fig. S4**) crystals were also refined by single crystal XRD. For the mixed-halide crystal, Br and Cl atoms randomly occupy distinct sites in the lattice, leading to different Cd-X bond lengths (**Supplementary Fig. S4a**). Supplementary Table S1 lists all derived crystallographic information. As mentioned in main text, these two compounds were found to undergo monoclinic (*Cc*) to orthorhombic (*Ama*2) phase transition. Given that the solid-solution series are isostructural, they are expected to have similar structural phase transitions. However, the low decomposition temperature makes the HTP of Cl-rich compounds inaccessible by structural characterization. Therefore, we use pure Br sample for a detailed discussion of the phase transition in crystallographic aspect.

In the low temperature phase (LTP), the crystal consists of edge-sharing 1D $CdBr_5^-$ hexahedron framework linked by PTMA cations through hydrogen bond between H in the methyl group and Br in the hexahedron. A simple polarization analysis can be made by treating N and Cd sites as the positive and negative charge centers, respectively. As shown in Supplementary Fig. S3a, there is a net polarization along the ***c*** direction, while in the ***b*** direction, the neighboring dipoles cancel out to give zero net polarization. Polarization along the ***a*** direction can be identified in Fig. 1c of the main text. However, due to the large size of the organic cation, polarization switching along this direction requires unrealistic high energy, which is confirmed by HTP crystallography and mm2Fm Aizu rule for the phase transition[1].

The structural transition of pure Br compound occurs at 19 °C. In the HTP, due to increasing thermal energy, the organic moieties become dynamically disordered between the two energy-equivalent states. To accommodate this structural change, the longest Cd-Br bond (bond length ~3.2 Å) within the inorganic chain is broken (red cross in **Supplementary Fig. S3a**). Consequently, Br1 and Br3 relocate into new energy-minimum sites, which has the same distance to the two neighboring Br2 atoms. The 1D inorganic chain then transforms into corner-sharing $CdBr_4^-$ tetrahedra with the restoration of mirror symmetry (denoted by red dash line in **Supplementary Fig. S3b**) and the loss of net polarization along the ***c*** axis.

PFM characterization

Polarization orientation of the 77%-Br crystal was investigated by PFM with the ***b*** axis perpendicular to the basal plane, that is, the polarization vector lies in plane. In-plane PFM measures torsional motion of the cantilever caused by shear piezoelectricity arising from in-plane polarization (P). The magnitude of the torsion (PFM amplitude) is proportional to the polarization component perpendicular to the cantilever axis, namely, $P \cdot cos\theta$, where θ is the azimuthal angle

between the cantilever axis and the *P* vector. Angle-resolved PFM study can then be conducted by rotating the sample in the basal plane to determine its *P* direction. To increase the signal-to-noise ratio, resonance-enhanced DART mode was used. Since the contact resonance and quality factor remain almost unchanged throughout the experiment, the raw amplitude data (A) were used for analysis. **Supplementary Fig. S5** shows the PFM images ($A\cos[phase]$) and corresponding average amplitude data at different azimuthal angles. By fitting these phase and amplitude signals, *P* direction can be determined as denoted by the red arrows. Particularly, A maximum is obtained at ~160° rather than at 0° and 180°, which is consistent with the non-zero polarization components along both the ***a*** and ***c*** axes.

Ferroelectric characterizations

Temperature dependent dielectric measurement was conducted on a 77%-Br single crystal to investigate dielectric anomaly across the phase transition. As shown in **Supplementary Fig. S6**, the dielectric anomaly along the ***c*** axis cannot be described by either peak-like or step-like behavior, possibly due to the mixed characters of both order-disorder and displacive type for this transition. The slight change in the ***a*** axis is attributed to the reduced molecular tilt in the HTP. No significant change was observed along the ***b*** axis.

Ferroelectric properties were investigated in details by temperature dependent hysteresis loop and positive-up-negative-down (PUND) measurements. 63%-Br sample was chosen due to its relatively high phase transition temperature (150° C) and ease in polarization switching. Hysteresis loops were first measured under different electric fields at a frequency of 2 Hz (**Supplementary Fig. S7a**). With electric field increasing to 5.1 kV/cm, P-E loop gradually becomes saturated with a remnant polarization (P_r) of 3.2 μC/cm^2. Polarization switching was then measured at different temperatures (**Supplementary Fig. S7b**). While P_r shows no obvious change

at higher temperatures, PE loops become narrower, indicating the reduction of switching barrier between two equivalent polarization states. PUND method was also employed to study the polarization switching kinetics (**Supplementary Fig. S7c, d**). Here, the switchable remnant polarization ($\Delta P_r=2P_r$) is calculated by subtracting the non-remnant components from the total switched polarization. Similar to conventional ferroelectrics that follow Merz's law, ΔP_r saturates at high electric field and long pulse width, and increasing temperature leads to the reduction of the onset pulse width for polarization switching, yet no obvious change in P_r value, which is consistent with the P-E loop data.

Large-signal dielectric response

To correlate with the "large signal" piezoelectric measurements, the dielectric responses of different samples were measured under high-field (0.1 – 1.7 kV/cm, lower than the coercive field) condition using polarization - electric field (P – E) curves. As a result, the dielectric loss cannot be obtained directly as those measured by conventional LCR meter using "small signal". The raw P – E data measured at 200 V (~1.7 kV/cm) are shown in **Supplementary Fig. S9a, b** for pure Cl and 90%-Br samples, respectively. Clearly, the P – E curves are consistent with a lossy capacitor response[2], especially for the Br-rich sample. Note that here the loss is due to domain wall motion/ferroelastic switching instead of leakage as the samples are highly insulating. For complex dielectric constant, $\varepsilon_r^* = \varepsilon_r' - i\varepsilon_r''$, the real part ε_r' contributes to the linear portion of the P – E curve, while the imaginary part ε_r'' results in dielectric loss, leading to the "blow-up" of the P-E curve. The overall P – E behaviour can be simulated by the Rayleigh law as proposed by Damjanovic et al.[3] using the following equations:

$$\varepsilon_r'(E_0) = \varepsilon_r'(0) + \alpha E_0 \quad (1)$$

$$P = \varepsilon_0 \left\{ [\varepsilon_r'(0) + \alpha E_0]E \pm \left(\frac{\alpha}{2}\right)(E_0^2 - E^2) \right\} \quad (2)$$

where $\varepsilon_r'(0)$ is the permittivity in the low field region and α is the Rayleigh coefficient (equal to the gradient of the ε_r' vs E plot). Then, the imaginary part ε_r'' is related to the Rayleigh coefficient α through:

$$\varepsilon_r'' = \frac{4}{3\pi}\alpha E_0 \quad (3)$$

Loss tangent is then calculated by

$$tan\delta = \frac{\varepsilon_r''}{\varepsilon_r'} \quad (4)$$

The calculated dielectric constant and loss versus frequency under various fields are shown in **Supplementary Fig. S10**. The Rayleigh-like behaviour of the dielectric response is consistent with the strong frequency and field dependence found in the piezoelectric responses, both of which are attributed to the slow motion of non-180° ferroelectric domain walls (ferroelastic switching in other words) in the crystal. By chemical substitution with Br, we effectively lower the ferroelastic switching barrier, and boost the piezoelectric response, though in a nonlinear manner. Further chemical engineering is required to flatten the energy landscape to achieve more linear response.

Supplementary Text 2 | Theoretical calculations

Polarization tensor

For the structure shown on the left side of Fig. 1c, the DFT calculated polarization vector is $(7.8 + nP_{\mathrm{Cl}}, 0, -3.7)$ μC/cm^2 for (PTMA)$CdCl_3$ and $(9.5 + mP_{\mathrm{Br}}, 0, -2.8)$ μC/cm^2 for (PTMA)$CdBr_3$. Here n and m are undetermined integers, $P_{\mathrm{Cl}} = 15.8$ and $P_{\mathrm{Br}} = 14.8$ mC/cm^2 are the polarization quantum defined as $\frac{1}{\Omega}ea$, where e is the electronic charge, a is the length of the lattice vector along the ***a*** axis, and Ω is the unit cell volume. The absolute magnitude of polarization along ***a*** cannot be fully determined, because no high-symmetry reference structure is available in this direction. On the other hand, the components of polarization along the ***b*** and ***c*** axis can be uniquely determined, since the structure is non-polar along ***b***, and the polarization can be switched along ***c***, such that an intermediate structure with zero P_c is well defined.

We have attempted to compute the molecular and inorganic contribution to the polarization, by rotating the PTMA molecules in 180 degrees with the rotational center at the N atom (assuming to be the center of charge of the molecule). However, due to the geometry of the molecule and the surrounding inorganic framework, some atoms become too close and the system is no longer insulating; hence the polarization (in particular the electronic contribution) cannot be calculated using the Berry's phase method. Considering that detailed contribution to the polarization is not the main focus of the manuscript, we may pursuit it in a future study.

Dielectric tensor

The DFPT calculated static dielectric tensor for (PTMA)$CdCl_3$ and (PTMA)$CdBr_3$, respectively, are

$$\begin{pmatrix} 2.88 & 0 & -0.01 \\ 0 & 2.86 & 0 \\ -0.01 & 0 & 2.58 \end{pmatrix} \text{ and } \begin{pmatrix} 3.01 & 0 & -0.01 \\ 0 & 3.00 & 0 \\ -0.01 & 0 & 2.77 \end{pmatrix}.$$

Nevertheless, we would like to emphasize that the large responses observed in experiment would not be reproduced by DFPT calculations. DFT calculations are mainly used to rationalize the effect of Br doping on the switching energy barrier and the bond strength, as well as to provide a rough estimation for the output stress in combination with the measured strain.

Elastic stiffness tensor

The elastic constants were calculated using the strain-stress relationship with finite differences[4]. Technically, IBRION=6, ISIF=3, and NFREE=4 were used in VASP. The elastic tensor is determined by performing six finite distortions of the lattice and calculating the corresponding stress.

To test the convergence with respect to energy cut-off, we carried out additional calculations with ENCUT varied from 500 to 800 eV. Many elastic constants may have rather sensitive dependence on the cut-off energy. For the relevant shear modulus C_{55}, as the applied electric field induces a shear strain and shear stress, a value of **5.8** GPa was obtained with high energy cut-off.

Regarding the computational details for elastic constants, according to the source code of VASP, a four-point method (NFREE=4) is used to extract the elastic constants from the strain-stress relationship, i.e., 4 unit-cell distortions are considered for each strain element. The size of the distortion is d=1.5%, and four distortions of -2d, - d, d, and 2d are performed. Then the elastic constant is evaluated as:

$$C_{ijkl} = \frac{-\sigma_{ij}(-2\delta_{kl}) + 8\sigma_{ij}(-\delta_{kl}) - 8\sigma_{ij}(\delta_{kl}) + \sigma_{ij}(2\delta_{kl})}{12\delta_{kl}}$$

where δ_{kl} is the 1.5% change of strain and σ_{ij} is the calculated stress. Voigt notation is then introduced to reduce the fourth-rank tensor C_{ijkl} to second rank. Please note that there is no stress/strain curve with this method. With ENCUT=800 eV, the elastic tensor (GPa) is

$$\begin{pmatrix} 26.2 & 8.1 & 9.4 & 0 & -1.0 & 0 \\ 8.1 & 29.6 & 7.8 & 0.3 & 0.3 & 0 \\ 9.4 & 7.8 & 21.5 & 0 & 0.2 & 0 \\ 0 & 0 & 0 & 6.1 & 0 & -0.3 \\ -1.0 & 0.3 & 0.2 & 0 & \mathbf{5.8} & 0 \\ 0 & 0 & 0 & -0.3 & 0 & 4.7 \end{pmatrix}.$$

Piezoelectric response under electric field

The DFT piezoelectric response was calculated by applying an electric field along the ***c*** axis, while only the ***a*** lattice vector was allowed to relax. Technically, the scheme of H. Fu and L. Bellaiche[5], is adopted, where the equilibrium geometry and coordinates are obtained by minimizing the electric enthalpy functional in the presence of an applied electric field, using the zero-field Born effective charge tensors. This setting is consistent with our experiment, as the bottom of the sample is fixed. As shown in **Supplementary Fig. 11**, when *the field is applied along the polarization direction*, d_{35} can be estimated as the slope of the shear strain *vs*. E-field, yielding 2.3 and 11.3 pC/N for (PTMA)$CdCl_3$ and (PTMA)$CdBr_3$, respectively. These values are significantly less than the estimation from experiments, suggesting that the giant piezoelectricity originates from the extrinsic effect of ferroelastic domain wall motion, instead of the intrinsic linear lattice deformation, as captured by DFT. The same finding is known in PZT and PMN-PT: the calculated "intrinsic" piezoelectric response strongly underestimates the experimentally measured one, owing to the dominant "extrinsic" contribution[6].

For *E-field applied opposite to the polarization direction*, DFT yields a large change of shear strain due to the ferroelastic switching. Remarkably, the change of the shear strain for

(PTMA)$CdCl_3$ (21.6 %) is very similar to the experimental value (22 %). The reduced coercive field from (PTMA)$CdBr_3$ can be attributed to the smaller switching energy barrier compared to that of (PTMA)$CdCl_3$. Please note that, due to Landauer's paradox[7], the electric field in simulation is usually larger compared with experiment.

Supplementary Text 3 | Calculations of the shear strain and piezoelectric coefficient, and calibration of the strain measurement setup

Equation for shear strain calculation

The shear strain was measured following the protocol described in Methods using the setup shown in Fig. 1b. The engineering shear strain is defined as $S = \tan\Delta\beta$. The small angle approximation of $tan\Delta\beta \approx \Delta\beta$ holds from small angles (the error for an angle below 15° is less than 2.3 %). For instance, taking the maximum $\Delta\beta$ = 12.6 ° in this work, $\tan(12.6\,°) = 0.2235 \cong radian(12.6\,°) = 0.2199$ with the error of 1.6 %. As a result, we can then calculate the shear strain by measuring the displacement *d* of the mirror fixed on the crystal using the approximation:

$$S = tan\Delta\beta \cong \Delta\beta = 2 \times \frac{\Delta\beta}{2} \cong 2tan\frac{\Delta\beta}{2} = 2 \times \frac{d/2}{H} = \frac{d}{H},$$

where *H* is the thickness of the crystal, ranging typically from 1 to 2 mm. This calculation method is also used in materials with comparable shear deformation, such as NiTi, the archetype shape memory alloy with shear strain up to 9 %[8].

Calculation of "large-signal" piezoelectric coefficient

By definition, piezoelectric coefficient d_{ij} can be expressed as

$$d_{ij} = (\frac{\partial D_i}{\partial T_j})^E = (\frac{\partial S_j}{\partial E_i})^T$$

where *D* is electric displacement, *T* is stress, *S* is the linearized strain and *E* is electric field. In this study, we use the latter definition, namely inverse piezoelectricity, to derive the coefficient. The unit conversion is

$$S\ (dimensionless)/E(in\frac{V}{m}) = d\ (in\frac{m}{V})$$

There are lots of reports that use the linear region of a nonlinear and/or hysteretic S-E curve to quantitatively calculate the piezoelectric coefficient[9, 10]. The problem of this method is, the slope changes under different field due to the hysteretic and/or nonlinear nature of the S-E curve. Therefore, in more general cases, people use S_{max}/E_{max} to calculate the so-called "large signal" piezoelectric coefficient d^* (E > kV/cm), to distinguish from the "small signal" one (E << kV/cm)[11-14]. In this study, we estimate the "large signal" d_{35}^* using S_{max}/E_{max}.

Calibration of the strain measurement setup

To confirm the reliability of our test system, we have measured repeatedly bipolar S-E hysteresis loops of a PMN-0.3PT (100) crystal in *33* mode (**Supplementary Fig. S8a**). **Supplementary Fig. S8b** shows the unipolar S-E curve of a pre-poled PMN-0.3PT (100) crystal in *33* mode, from which the large-signal d_{33}^* can be derived. The obtained value is comparable to literature reports[15, 16]. Fig. 3e shows the comparison of the bipolar S-E loops between PMN-PT and our sample. Due to the two order of magnitude difference, the data was shown in logarithm scale. The contrasting S-E hysteresis loops demonstrate completely different switching mechanisms in these two types of ferroelectrics. Moreover, we have also measured the unipolar shear S-E response of PMN-PT in 15 mode, using the same experimental setup (**Fig. 3f**). The obtained d_{15}^* of the pre-poled PMN-0.3PT (111) crystal agrees with previous reports[17, 18], again, confirming the reliability of the measurement setup. The piezoelectric coefficients of the commercial PMN-PT single crystal (CTG Advanced Materials, LLC, Formerly Operated as H.C. Materials, Acquired by CTS Corporation) can be found online for reference (http://www.hcmat.com/Pmn_Opportunities.html).

Supplementary Figures

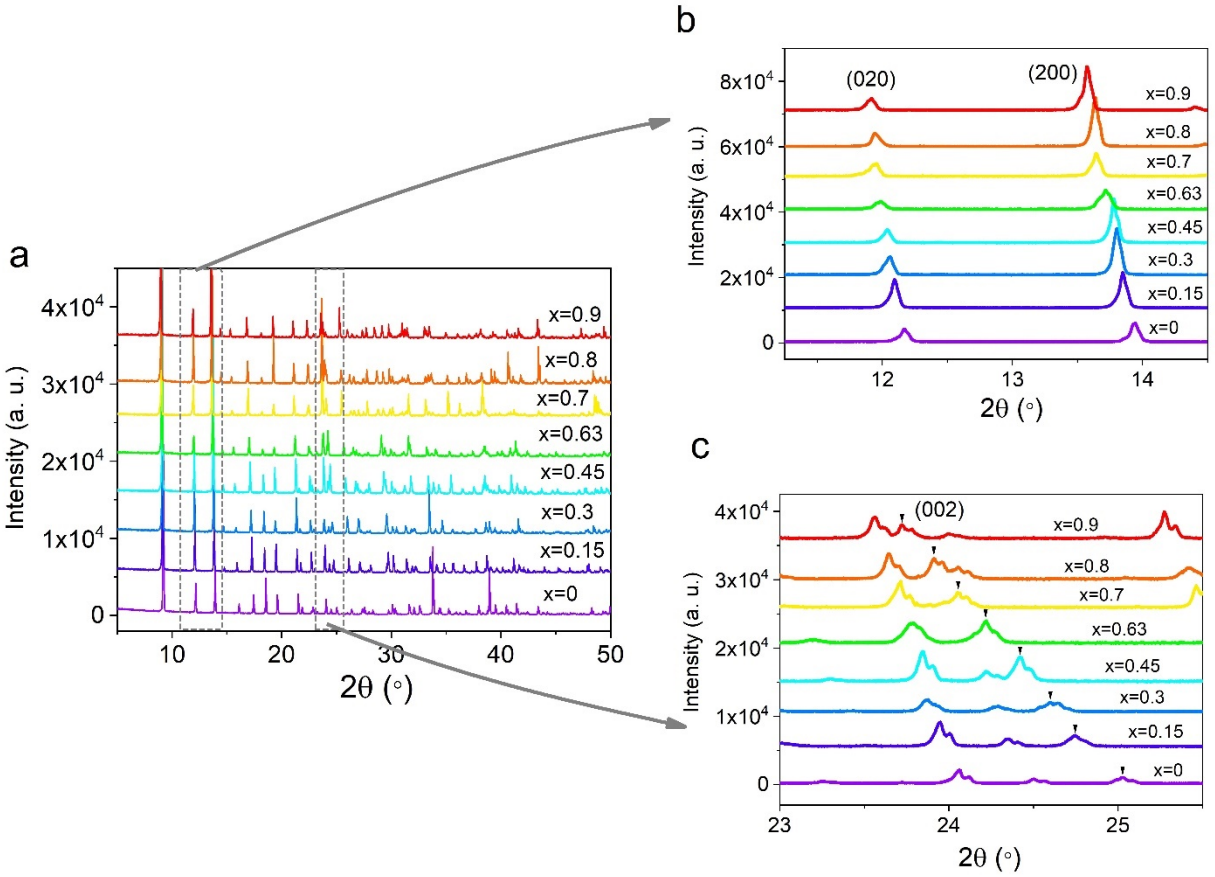

Supplementary Figure S1 | Powder XRD data. (**a**) Powder XRD patterns of (PTMA)$CdBr_{3x}Cl_{3(1-x)}$ with different halide compositions at room temperature. Zoomed-in XRD patterns (**b**) around (020) and (200) peaks, and (**c**) around (002) peak.

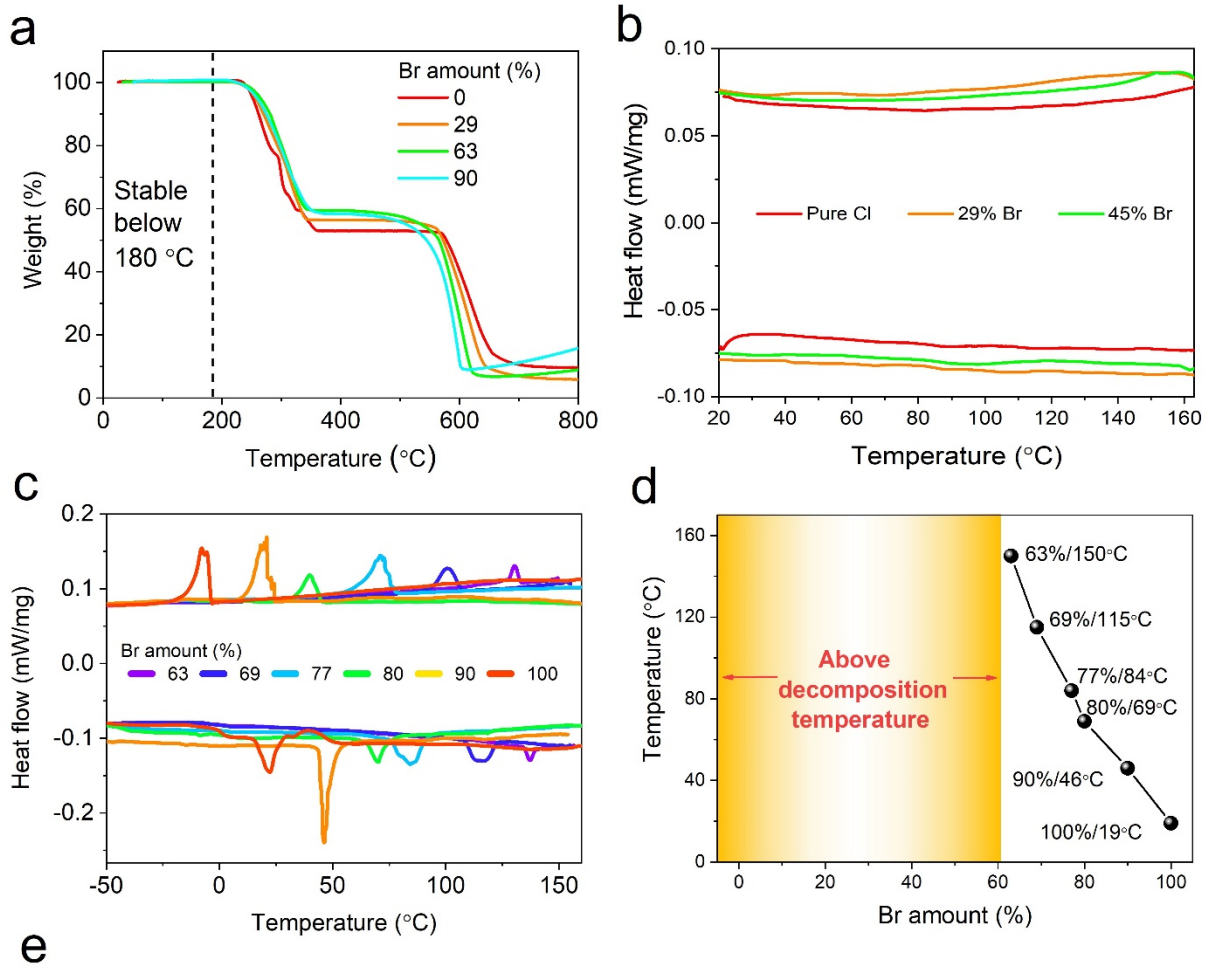

e

	Space group	a / Å	b / Å	c / Å	β / °	Volume (Å^3)	R factor (%)
RT 1	*Cc*	12.7404(4)	14.4928(6)	7.1432(3)	96.3055(14)	1310.97(9)	3.29
RT 2	*Cc*	12.7403(7)	14.4947(8)	7.1426(3)	96.2944(18)	1311.05(12)	4.03
140 °C	*Cc*	12.8037(8)	14.5316(11)	7.2085(5)	95.989(2)	1333.88(16)	6.41

Supplementary Figure S2 | Thermal analyses data. (**a**) TGA analyses of (PTMA)$CdBr_{3x}Cl_{3(1-x)}$ single crystals with different halide compositions, indicating good thermal stability below 180 °C. (**b**) DSC data of pure Cl and Br-poor crystals showing no phase transition up to 160 °C. (**c**) DSC curves of heating-cooling cycles for Br-rich samples. (**d**) Phase transition temperatures (heating cycle) of (PTMA)$CdBr_{3x}Cl_{3(1-x)}$ with different Br amounts. (**e**) Summary of the RT and HT crystallographic data of pure Cl crystal.

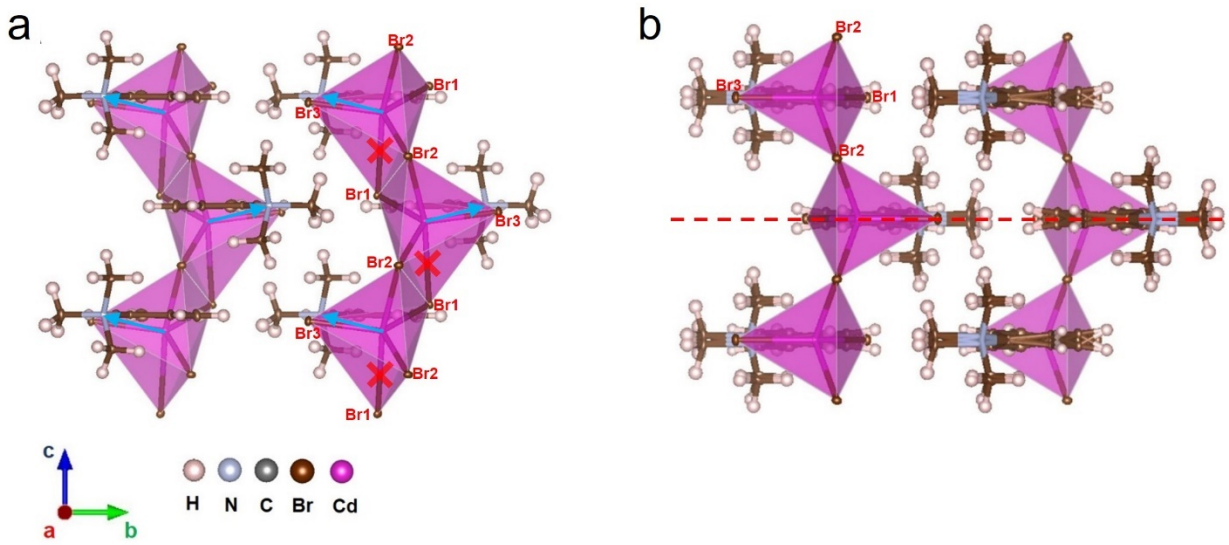

Supplementary Figure S3 | Crystal structures of pure Br compound viewed along the *a* axis. (**a**) LTP and (**b**) HTP. The blue arrows denote the electric dipoles. The broken bond during high-temperature phase transition is indicated by the red cross. The red dash line denotes the mirror plane of the HTP.

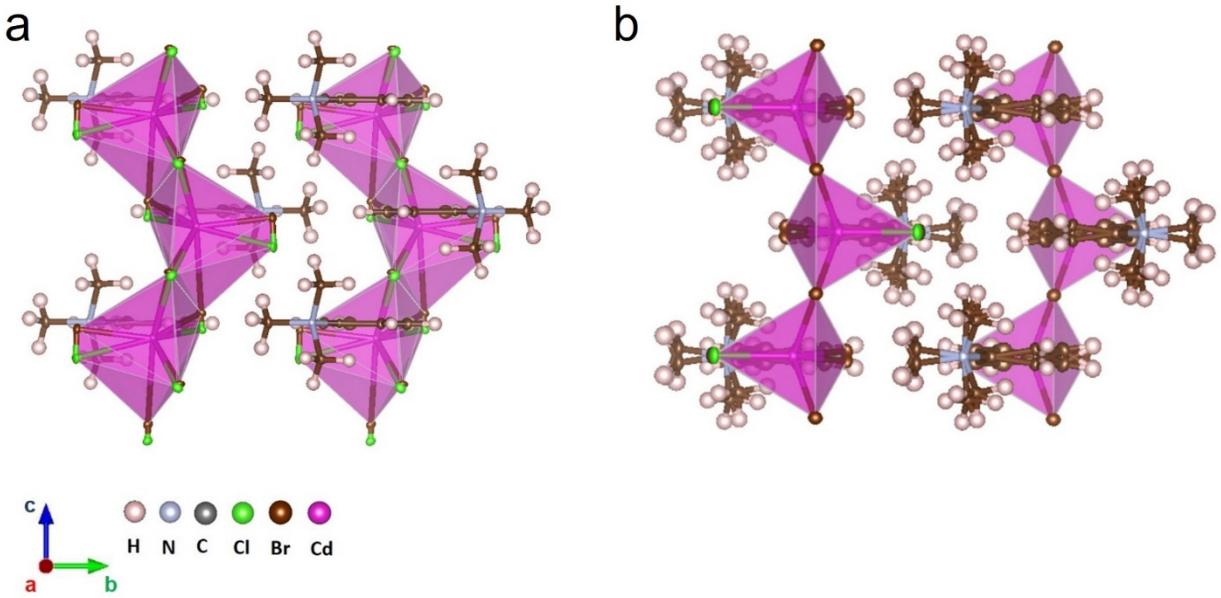

Supplementary Figure S4 | Crystal structures of 76%-Br sample viewed along the *a* axis. (**a**) LTP and (**b**) HTP.

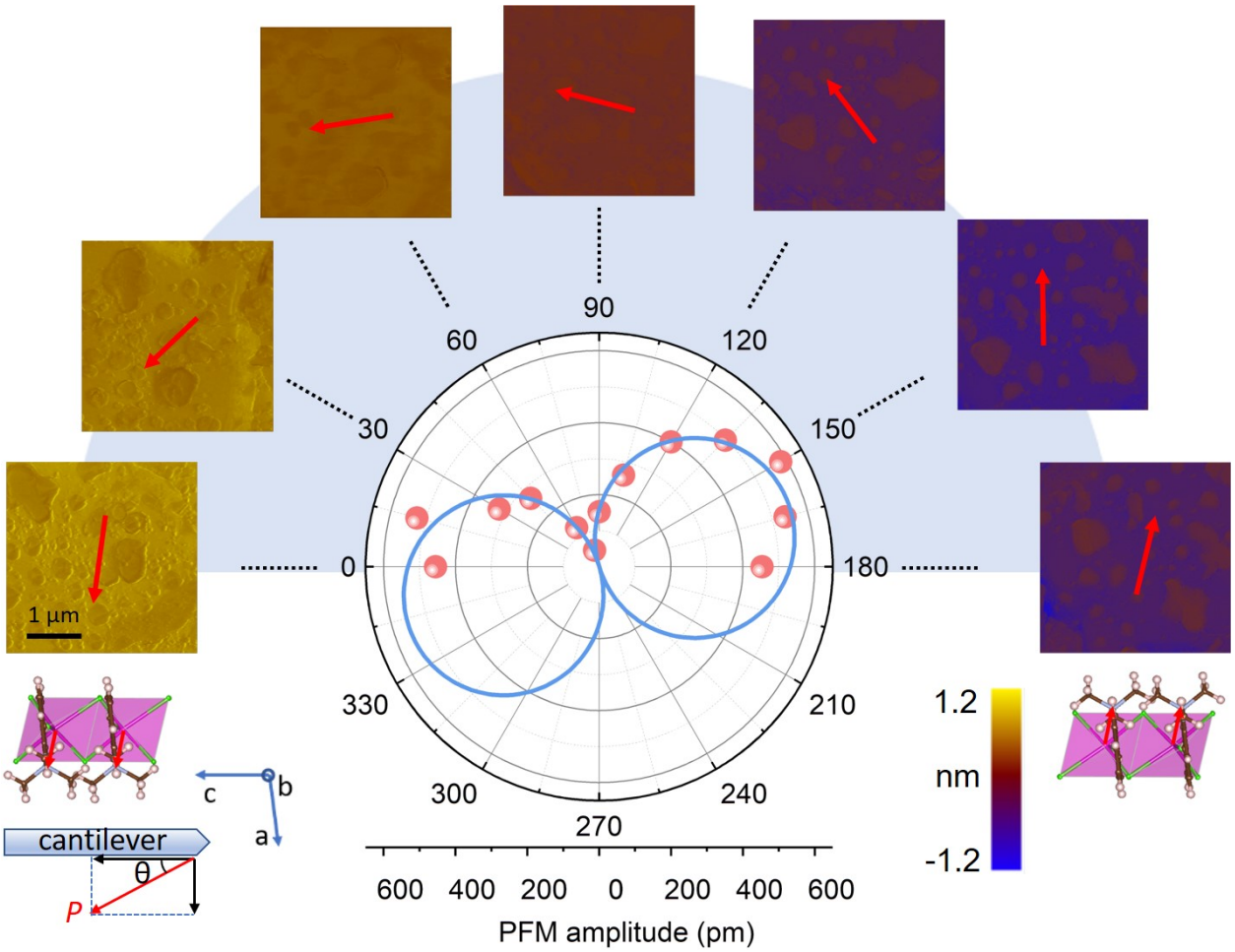

Supplementary Figure S5 | Angle-resolved in-plane PFM study of a 77%-Br single crystal. PFM images are collected with the crystal oriented at different azimuthal angles with regard to the cantilever axis. The average PFM amplitude of each image is plotted in polar coordinate. Initial and final crystallographic orientations are indicated beneath the PFM images, with red arrow denotes the polarization vector.

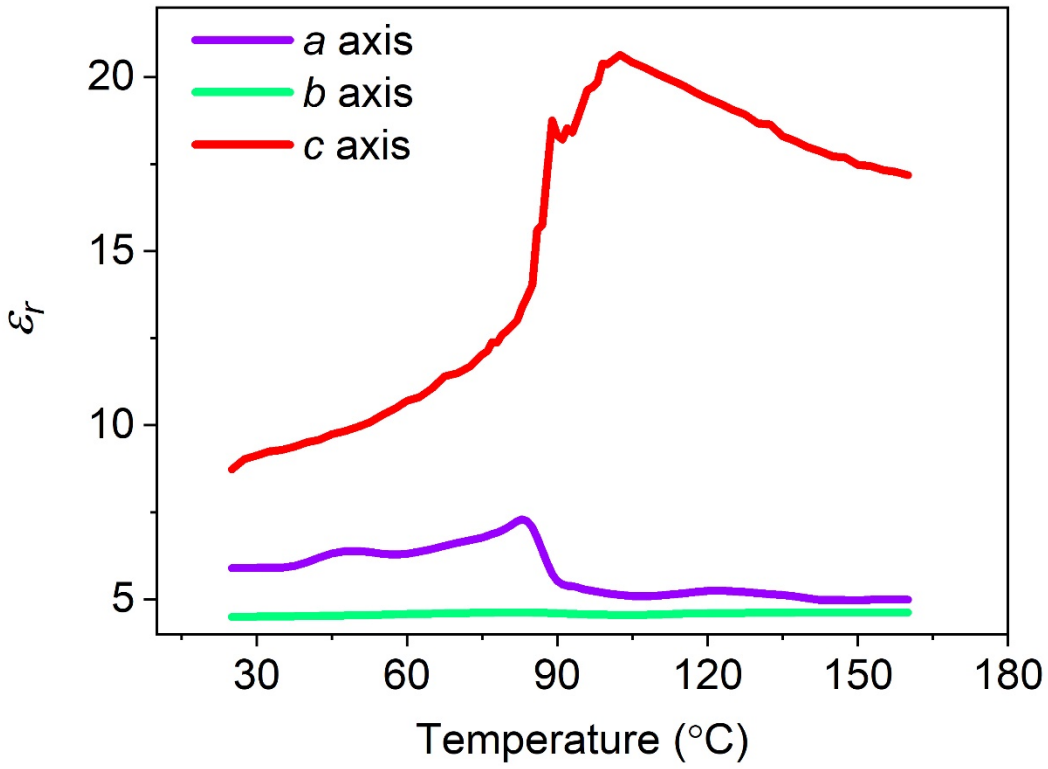

Supplementary Figure S6 | Dielectric response around the phase transition. Temperature dependent dielectric response of a 77%-Br crystal along different crystallographic axes upon heating measured at a frequency of 1 kHz.

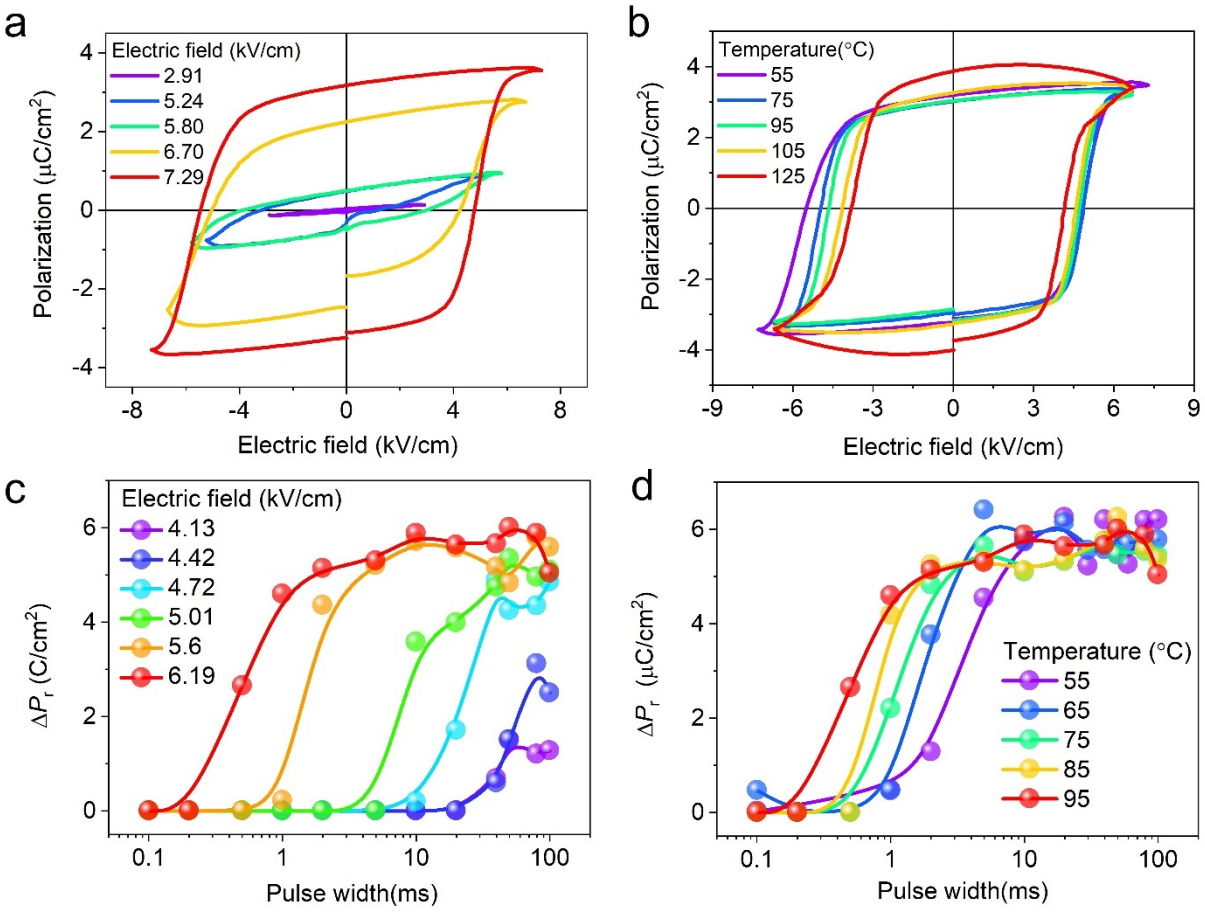

Supplementary Figure S7 | Polarization switching characteristics of a 63%-Br crystal. (**a**) Hysteresis loops under different electric fields at 55 °C. (**b**) Temperature dependent P - E loops. The frequency of P - E loop measurement is 2 Hz. (**c**) Electric field dependent PUND measurements at 95 °C. (**d**) PUND measurements at different temperatures under an electric field of 6.19 kV/cm.

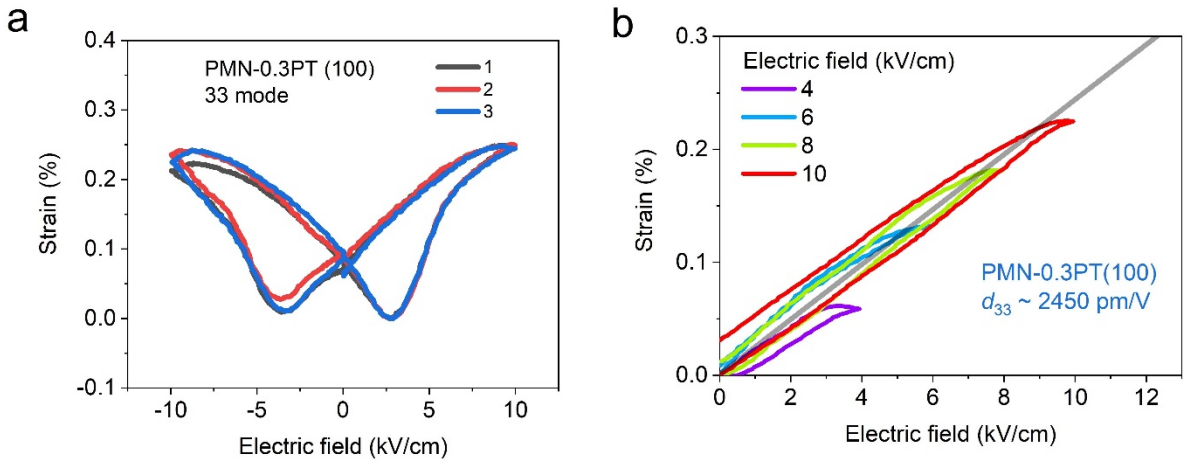

Supplementary Figure S8 | Benchmarking of the measurement setup and calculation of the piezoelectric coefficients. (**a**) Repetitive bipolar S-E curves of a PMN-0.3PT (100) crystal in 33 mode. (**b**) Unipolar S-E response of PMN-0.3PT (100) crystal under different electric fields in 33 mode. The slope of the linear fit is used to extract d_{33}.

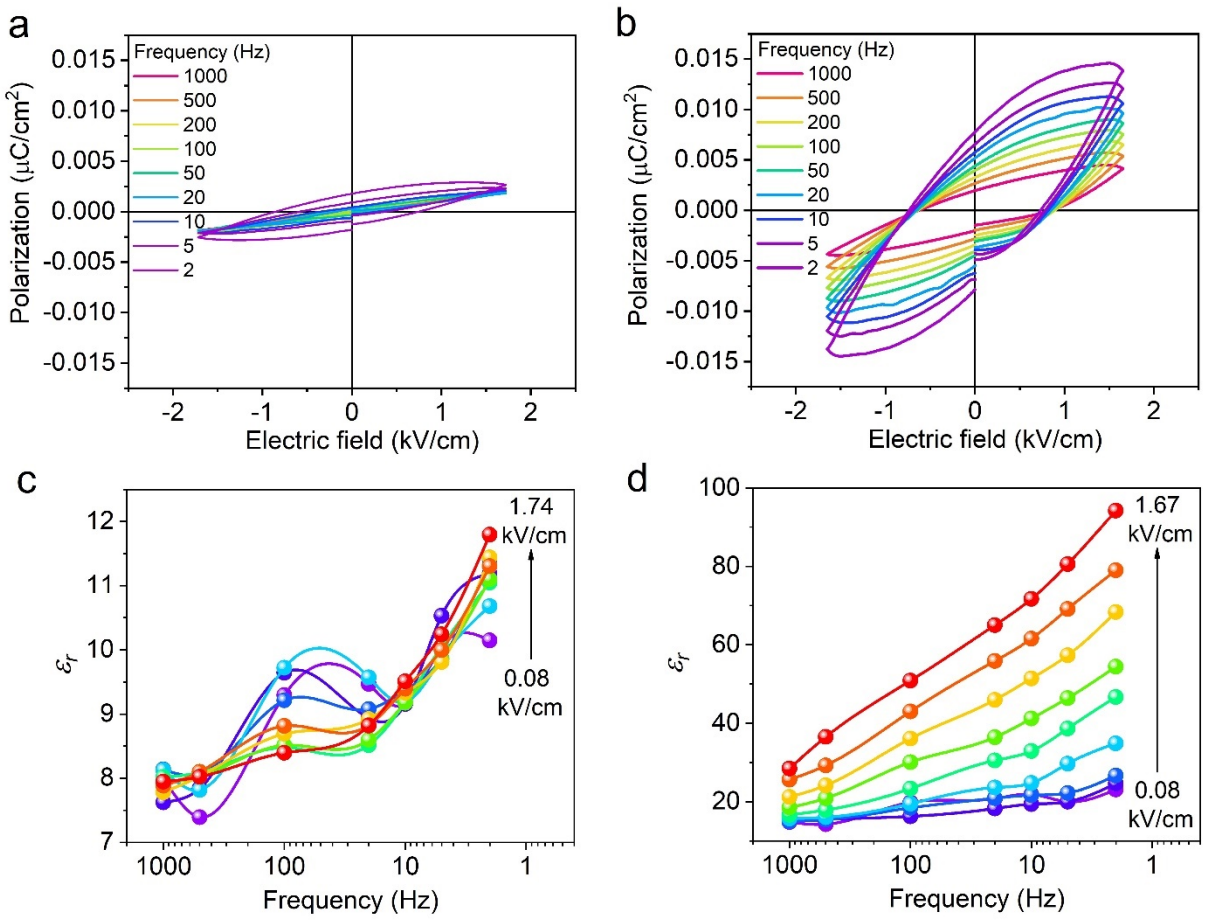

Supplementary Figure S9 | Large-signal dielectric response. Frequency dependent P – E curves (below coercive field) of (**a**) pure Cl sample measured at 1.74 kV/cm and (**b**) 90%-Br sample measured at 1.67 kV/cm. Calculated relative dielectric constants of (**c**) pure Cl sample and (**d**) 90%-Br sample at different frequencies and fields.

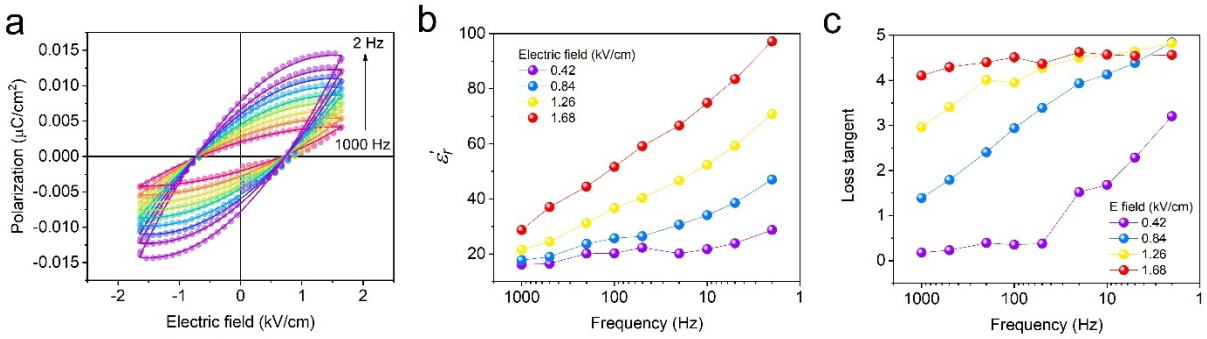

Supplementary Figure S10 | Fitting the large-signal dielectric response by Rayleigh law. (**a**) Below-coercive-field P – E curves of 90 %-Br sample fitted by Rayleigh law. (**b**) Derived real part of the dielectric constant from the fit. (**c**) Derived loss tangent from the fit. See Supplementary Text 1 for details.

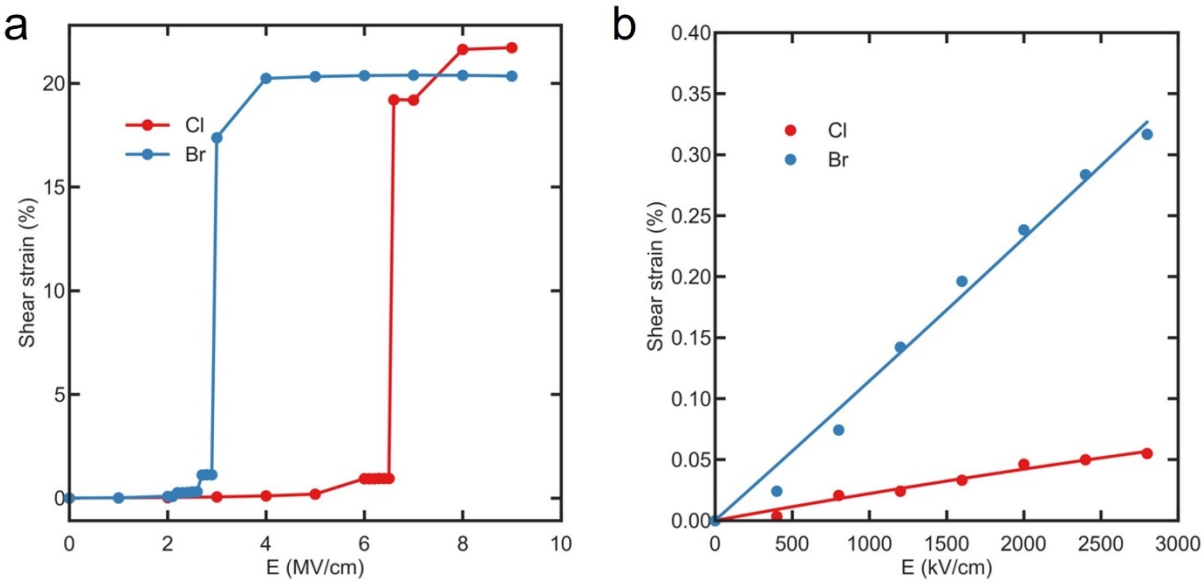

Supplementary Figure S11 | DFT calculated shear strain vs. electric field. (**a**) E-field opposite to the polarization direction. (**b**) E-field along the polarization direction. (see Supplementary Text 2 for detailed description).

Supplementary Tables

Supplementary Table S1 | Crystallographic data of (PTMA)$CdBr_{3X}Cl_{3(1-X)}$ with different Br amounts.

Br amount (%)	0	76		100	
Empirical formula	(PTMA)$CdCl_3$	(PTMA)$CdBr_{2.3}Cl_{0.7}$		(PTMA)$CdBr_3$	
Temperature (K)	299(2)	296(2)	393(2)	253(2)	308(2)
Space group	Cc	Cc	Ama2	Cc	Ama2
a (Å)	12.7404(4)	12.9705(15)	12.9801(13)	13.0388(5)	13.0309(9)
b (Å)	14.4928(6)	14.7252(17)	14.7100(14)	14.7738(6)	14.7328(9)
c (Å)	7.1432(3)	7.4093(8)	7.6583(6)	7.4720(3)	7.7137(4)
β (°)	96.3055(14)	95.121(4)	90	95.2538(10)	90
Volume ($Å^3$)	1310.97(9)	1409.48	1462.25	1433.3	1480.89
Z	4	4	4	4	4
F (000)	696	861	859	912	912
R factor (%)	3.29	3.8	3.15	3.71	3,88
Goodness-of-fit	1.029	1.036	1.009	1.072	1.064

Supplementary Table S2 | Actuation properties of different material systems

Material system	Compound	Strain (%)	Stress (MPa)	Strain type	Work per volume J/m^3	Power per volume W/m^3	Frequency (Hz)	Reference
Hybrid ferroelectric	$(PTMA)CdCl_3$	21.5	40	Shear	4.2×10^6	8.4×10^6	1-2	This work
Piezoelectric oxides	Soft PZT	0.1	20	Shear	2×10^4	2×10^5	10	[19]
	PMN-0.3PT	0.4	35	Normal	7×10^4	7×10^5	10	[20]
	BNT-BT-KNN	0.22	120	Normal	1.3×10^5	6.5×10^6	50	[21]
	PMN-0.38PT	0.66	20	Normal	6.6×10^4	6.6×10^6	100	[22]
	BTO	0.93	6	Normal	3.7×10^4	3.7×10^7	1000	[22]
Shape memory alloy	NiTi	8	700	Normal	2.8×10^7	—	—	[23-25]
	NiTiHf	3.5	150	Shear	5.25×10^6	—	—	[26]
	CuZnAl	4	550	Normal	1×10^7	—	—	[23-25]
	CuAlNi	4	450	Normal	9×10^6	—	—	[23-25]
MSMAs	NiMnGaCoCu	12	2	Normal	1.7×10^5	—	—	[27]
	14M NiMnGa	9.5	1.8	Normal	1.45×10^5	—	—	[28]
	NiFeGaCo	8.5	8.5	Normal	7.225×10^5	—	—	[29]
Shape memory polymer	Polyurethane	80	0.05	Normal	2×10^4	20	1×10^{-3}	[30]
	Styrene resin	30	0.236	Shear	3.5×10^4	35	1×10^{-3}	[31]
	Semicrystalline oligome	50	0.5	Shear	1.2×10^5	120	1×10^{-3}	[32]
	Nylon 66	10	22	Normal	1×10^6	5×10^6	1-5	[33]
Electroactive polymers	Graft elastomer	4	22	Normal	4.4×10^5	4.4×10^7	100	[34]
	Polyurethane	11	2	Normal	1.1×10^5	1.1×10^7	100	[34]

	VHB 4910 acrylic	68	2.4	Normal	1.36×10^{6}	5.4×10^{7}	40	[35]
	HS3 silicone	54	0.4	Normal	1.6×10^{5}	3.2×10^{8}	2000	[35]
	CF19-2186	39	0.8	Normal	2×10^{5}	3.4×10^{7}	170	[35]
	Liquid crystal	4	0.12	Normal	2.4×10^{3}	2.4×10^{5}	100	[36]
	Polypyrrole	5	1.2	Normal	3×10^{4}	3×10^{2}	0.01	[37]
Piezoelectric polymer	PVDF	1.6	35	Normal	2.8×10^{5}	5.6×10^{5}	2	[38]
	PVDF+CuPc	2	15	Normal	1.5×10^{5}	1.5×10^{5}	1	[39]
	Irradiated PVDF	4	15	Normal	3×10^{5}	3×10^{6}	1-10	[40]

Supplementary Table S3 | Shear piezoelectric properties of different materials.

Compound	Piezoelectric coefficient (pm/V)	Piezoelectric mode	Reference
$(PTMA)CdBr_{2.7}Cl_{0.3}$	~4830	d_{35}*	This work
KH_2PO_4	23.2	d_{36}	41
$LiNbO_3$	68	d_{15}	41
PbTiO3	68	d_{15}	42
Glycine amino acid (β)	178	d_{16}	43
$BaTiO_3$	260	d_{15}	41
PZT-5A	584	d_{35}	44
BZT-BCT	1586	d_{36}	45
$(TMFM)_{0.26}(TMCM)_{0.74}CdCl_3$	2560	d_{15}	46
Pb based relaxors	1300-5000	d_{15}	47

Supplementary Table S4 | Calculated bond lengths and integrated crystal orbital Hamilton populations (ICOHP). The integration is done up to the Fermi energy for (1) the X-Cd bond that breaks during switching, (2) the shortest (X-H1) and (3) the second shortest hydrogen bond for pure Cl and pure Br structures.

Bond	Bond length (Å)	ICOHP (eV)
Cd-Cl	2.81760	-0.59455
Cl-H1	2.61135	-0.12741
Cl-H2	2.71702	-0.13675
Cd-Br	3.02990	-0.47219
Br-H1	2.69734	-0.09563
Br-H2	2.84170	-0.12472

Captions for Supplementary Movies

Movie S1 | Real-time video of the ferroelastic switching cycle of a bulk (PTMA)$CdBr_{0.45}Cl_{2.55}$ single crystal at a frequency of 1 Hz. (starting from left-tilt to right-tilt, and back to left-tilt).

Movie S2 | Real-time video of the ferroelastic switching cycle of a bulk (PTMA)$CdBr_{0.45}Cl_{2.55}$ single crystal at a frequency of 1 Hz. (starting from right-tilt to left-tilt, and back to right-tilt).

Movie S3 | Real-time video of the ferroelastic switching cycles of a bulk (PTMA)$CdBr_{2.7}Cl_{0.3}$ single crystal at frequencies ranging from 0.5 – 20 Hz.

Movie S4 | Structural evolution of (PTMA)$CdCl_3$ during the ferroelastic switching as derived from the switching path calculation.

Movie S5 | Structural evolution of (PTMA)$CdBr_3$ during the ferroelastic switching as derived from the switching path calculation.

References

1. Aizu, K. Possible species of "ferroelastic" crystals and of simultaneously ferroelectric and ferroelastic crystals. *J. Phys. Soc. Jpn.* **27**, 387-396 (1969).
2. Dawber, M., Rabe, K.M. & Scott, J.F. Physics of thin-film ferroelectric oxides. *Rev. Mod. Phys.* **77**, 1083-1130 (2005).
3. Damjanovic, D. & Demartin, M. The Rayleigh law in piezoelectric ceramics. *J. Phys. D: Appl. Phys.* **29**, 2057-2060 (1996).
4. Le Page, Y. & Saxe, P. Symmetry-general least-squares extraction of elastic data for strained materials from ab initio calculations of stress. *Phys. Rev. B* **65**, 104104 (2002).
5. Fu, H. & Bellaiche, L. First-principles determination of electromechanical responses of solids under finite electric fields. *Phys. Rev. Lett.* **91**, 057601 (2003).
6. Bellaiche, L. & Vanderbilt, D. Intrinsic piezoelectric response in perovskite alloys: PMN-PT versus PZT. *Phys. Rev. Lett.* **83**, 1347-1350 (1999).
7. Landauer, R. Electrostatic considerations in $BaTiO_3$ domain formation during polarization reversal. *J. Appl. Phys.* **28**, 227-234 (1957).
8. Orgéas, L. & Favier, D. Stress-induced martensitic transformation of a NiTi alloy in isothermal shear, tension and compression. *Acta Mater.* **46**, 5579-5591 (1998).
9. Park, S.-E. & Shrout, T.R. Ultrahigh strain and piezoelectric behavior in relaxor based ferroelectric single crystals. *J. Appl. Phys.* **82**, 1804-1811 (1997).
10. Liu, W. & Ren, X. Large piezoelectric effect in Pb-free ceramics. *Phys. Rev. Lett.* **103**, 257602 (2009).
11. Viehland, D. *et al.* Effect of uniaxial stress on the large-signal electromechanical properties of electrostrictive and piezoelectric lead magnesium niobate lead titanate ceramics. *J. Appl. Phys.* **95**, 1969-1972 (2004).
12. Zhang, S.-T., Kounga, A.B., Aulbach, E., Ehrenberg, H. & Rödel, J. Giant strain in lead-free piezoceramics $Bi_{0.5}Na_{0.5}TiO_3$–$BaTiO_3$–$K_{0.5}Na_{0.5}NbO_3$ system. *Appl. Phys. Lett.* **91**, 112906 (2007).
13. Kerkamm, I., Hiller, P., Granzow, T. & Rödel, J. Correlation of small- and large-signal properties of lead zirconate titanate multilayer actuators. *Acta Mater.* **57**, 77-86 (2009).
14. Hao, J., Li, W., Zhai, J. & Chen, H. Progress in high-strain perovskite piezoelectric ceramics. *Mater. Sci. Eng. R Rep.* **135**, 1-57 (2019).
15. Li, F. *et al.* Composition and phase dependence of the intrinsic and extrinsic piezoelectric activity of domain engineered $(1-x)Pb(Mg_{1/3}Nb_{2/3})O_3-xPbTiO_3$ crystals. *J. Appl. Phys.* **108**, 034106 (2010).
16. Li, F. *et al.* Giant piezoelectricity of Sm-doped $Pb(Mg_{1/3}Nb_{2/3})O_3$-$PbTiO_3$ single crystals. *Science* **364**, 264-268 (2019).
17. Zhang, R., Jiang, B. & Cao, W. Single-domain properties of $0.67Pb(Mg_{1/3}Nb_{2/3})O_3$–$0.33PbTiO_3$ single crystals under electric field bias. *Appl. Phys. Lett.* **82**, 787-789 (2003).
18. Han, P., Yan, W., Tian, J., Huang, X. & Pan, H. Cut directions for the optimization of piezoelectric coefficients of lead magnesium niobate–lead titanate ferroelectric crystals. *Appl. Phys. Lett.* **86**, 052902 (2005).
19. Glazounov, A.E., Zhang, Q.M. & Kim, C. Torsional Actuator and Stepper Motor Based on Piezoelectric d15 Shear Response. *J. Intell. Mater. Syst. Struct.* **11**, 456-468 (2000).
20. Viehland, D. & Powers, J. Effect of uniaxial stress on the electromechanical properties of $0.7Pb(Mg_{1/3}Nb_{2/3})O_3$–$0.3PbTiO_3$ crystals and ceramics. *J. Appl. Phys.* **89**, 1820-1825 (2001).
21. Dittmer, R., Aulbach, E., Jo, W., Webber, K.G. & Rödel, J. Large blocking force in Bi1/2Na1/2TiO3-based lead-free piezoceramics. *Scripta Mater.* **67**, 100-103 (2012).
22. Burcsu, E., Ravichandran, G. & Bhattacharya, K. Large strain electrostrictive actuation in barium titanate. *Appl. Phys. Lett.* **77**, 1698-1700 (2000).
23. Welsch, G., Boyer, R. & Collings, E.W. *Materials Properties Handbook: Titanium Alloys*. (ASM International, 1993).
24. Otsuka, K. & Wayman, C.M. *Shape Memory Materials*. (Cambridge University Press, 1999).

25. Huang, W. On the selection of shape memory alloys for actuators. *Mater. Des.* **23**, 11-19 (2002).
26. Hayrettin, C. *et al.* Two way shape memory effect in NiTiHf high temperature shape memory alloy tubes. *Acta Mater.* **163**, 1-13 (2019).
27. Sozinov, A., Lanska, N., Soroka, A. & Zou, W. 12% magnetic field-induced strain in Ni-Mn-Ga-based non-modulated martensite. *Appl. Phys. Lett.* **102**, 021902 (2013).
28. Sozinov, A., Likhachev, A.A., Lanska, N. & Ullakko, K. Giant magnetic-field-induced strain in NiMnGa seven-layered martensitic phase. *Appl. Phys. Lett.* **80**, 1746-1748 (2002).
29. Morito, H. *et al.* Stress-assisted magnetic-field-induced strain in Ni–Fe–Ga–Co ferromagnetic shape memory alloys. *Appl. Phys. Lett.* **90**, 062505 (2007).
30. Tobushi, H., Okumura, K., Endo, M. & Hayashi, S. Thermomechanical properties of polyurethane-shape memory polymer foam. *J. Intell. Mater. Syst. Struct.* **12**, 283-287 (2001).
31. Li, G. & Nettles, D. Thermomechanical characterization of a shape memory polymer based self-repairing syntactic foam. *Polymer* **51**, 755-762 (2010).
32. Michal, B.T., Spencer, E.J. & Rowan, S.J. Stimuli-responsive reversible two-level adhesion from a structurally dynamic shape-memory polymer. *ACS Appl. Mater. Interfaces* **8**, 11041-11049 (2016).
33. Haines, C.S. *et al.* Artificial muscles from fishing line and sewing thread. *Science* **343**, 868-872 (2014).
34. Su, J., Harrison, J.S., Clair, T.L.S., Bar-Cohen, Y. & Leary, S. Electrostrictive graft elastomers and applications. *MRS Proceedings* **600**, 131 (2011).
35. Pelrine, R., Kornbluh, R., Pei, Q. & Joseph, J. High-speed electrically actuated elastomers with strain greater than 100%. *Science* **287**, 836-839 (2000).
36. Lehmann, W. *et al.* Giant lateral electrostriction in ferroelectric liquid-crystalline elastomers. *Nature* **410**, 447-450 (2001).
37. Spinks, G.M., Liu, L., Wallace, G.G. & Zhou, D. Strain response from polypyrrole actuators under load. *Adv. Funct. Mater.* **12**, 437-440 (2002).
38. Wang, Y., Ren, K. & Zhang, Q.M. Direct piezoelectric response of piezopolymer polyvinylidene fluoride under high mechanical strain and stress. *Appl. Phys. Lett.* **91**, 222905 (2007).
39. Zhang, Q.M. *et al.* An all-organic composite actuator material with a high dielectric constant. *Nature* **419**, 284-287 (2002).
40. Zhang, Q.M., Bharti, V. & Zhao, X. Giant electrostriction and relaxor ferroelectric behavior in electron-irradiated poly(vinylidene fluoride-trifluoroethylene) copolymer. *Science* **280**, 2101-2104 (1998).
41. Tressler, J.F., Alkoy, S. & Newnham, R.E. Piezoelectric sensors and sensor materials. *J. Electroceramics* **2**, 257-272 (1998).
42. Turner, R.C., Fuierer, P.A., Newnham, R.E. & Shrout, T.R. Materials for high temperature acoustic and vibration sensors: a review. *Appl. Acoust.* **41**, 299-324 (1994).
43. Guerin, S. *et al.* Control of piezoelectricity in amino acids by supramolecular packing. *Nat. Mater.* **17**, 180-186 (2018).
44. Altammar, H., Dhingra, A. & Salowitz, N. Ultrasonic sensing and actuation in laminate structures using bondline-embedded d_{35} piezoelectric sensors. *Sensors* **18** (2018).
45. Berik, P., Chang, W.-Y. & Jiang, X. *Piezoelectric torsional actuation in d_{36} shear-mode PMN-PT single crystals*, Vol. 10598. (SPIE, 2018).
46. Liao, W.-Q. *et al.* A molecular perovskite solid solution with piezoelectricity stronger than lead zirconate titanate. *Science* **363**, 1206-1210 (2019).
47. Li, F., Zhang, S., Xu, Z., Wei, X. & Shrout, T.R. Critical property in relaxor-$PbTiO_3$ single crystals – shear piezoelectric response. *Adv. Funct. Mater.* **21**, 2118-2128 (2011).